Ensemble Monte Carlo simulation for electron transport in quantum wire structures

Yuji Ando[a] and Alain Cappy
Institut d'électronique et de microélectronique du nord, 59655 Villeneuve d'Ascq Cédex, France

(Received 25 January 1993; accepted for publication 4 June 1993)

Ensemble Monte Carlo simulations are performed for the GaAs (100) oriented square well wire. The model considers the infinite potential approximation as well as the extreme confinement limit, i.e., one-dimensional subbands are formed in the L and X valleys as well as in the Γ valley. We discuss the electron dynamics in quantum wire structures from steady-state, transient, and diffusion aspects. Even at very low electric fields (10–100 V/cm), the non-Maxwellian distribution, originating from the one-dimensional density of states, leads to electron heating and a deviation from the Einstein relation, as well as mobility enhancement. At high fields, the anisotropic mass effects of the satellite valleys gives rise to a saturation velocity enhancement as well as a diffusivity increase. The low-temperature simulations show temporal oscillations of velocity due to the periodical phonon emissions. This effect possibly suppresses the diffusion noise, since no additional carrier diffusion is introduced with a periodic velocity oscillation. The velocity overshoot phenomena are studied based on the relaxation time approximation and are compared to the transient Monte Carlo results. The satisfactory agreement obtained between these two results indicates the validity of the phenomenological approach to quantum wire structures.

I. INTRODUCTION

In the trend of III-V transport device developments, carrier confinement has been intensified from three-dimensional (3-D) in metal-semiconductor field-effect transistors (MESFETs) to two-dimensional (2-D) in high electron mobility transistors (HEMTs). To avoid the future limitations of present devices, one possible solution can be a further reduction of the carrier dimension, i.e., the application of one-dimensional (1-D) systems. Recent progress in lithography and crystal growth techniques has enabled the fabrication of ultrafine structures. As a result, there have been considerable reports examining novel devices employing quasi-1-D channels.[1–5]

Many theoretical works have investigated carrier transports in quantum wire (QWI) structures. Sakaki predicted a significant enhancement of 1-D mobility arising from a suppression of Coulomb scatterings as a result of limiting the number of final states.[6] Since Sakaki's proposal, several scattering mechanisms, e.g., polar-optical,[7,8] surface-optical,[9] acoustical,[10] and Coulomb[11–14] interactions, have been studied for 1-D systems. Recently, several authors have reported Monte Carlo simulations for QWIs.[15–18] An alternate approach, directly solving the Boltzmann equation, was also reported.[19]

Most of the previous theoretical works have been focused on steady-state behaviors in 1-D transports. However, the nonstationary transport phenomenon, as well as carrier diffusion, becomes essential in ultrasmall devices for microwave applications. The purpose of our paper is to investigate the steady-state, transient, and diffusion dynamics in QWIs. The ensemble Monte Carlo (EMC) technique is utilized for simulating electron transports in the GaAs QWI structure. The model considers both an infinite square well potential and the extreme confinement limit, i.e., 1-D subbands are formed in the L and X valleys as well as in the Γ valley. Seemingly, this assumption is not suited for the present quasi-1-D devices. Our main interest is, however, in the potential performance of QWI structures. Features of our simulation are the following: (i) The standard three valley configuration is employed. (ii) 32 subbands (the lowest four subbands in each valley) are simulated. (iii) The anisotropic effects in the L and X valleys as well as the nonparabolicity in the Γ valley are taken into account. (iv) The polar optical phonon (POP) and intervalley deformation potential scatterings are included. (v) Degeneracy effects are introduced.

The band structure dealt with here will be described in Sec. II. In Secs. III and IV, we shall outline the procedures for the 1-D scattering rate calculations and the Monte Carlo simulations, respectively. The steady-state simulation results will be described in Sec. V; Sec. VI will report the transient simulation results comparing to the phenomenological theory findings. Finally, in Sec. VII, we shall report the electron diffusion in QWI structures.

II. BAND STRUCTURE

Figure 1 illustrates the QWI structure studied in this paper. We deal with the GaAs QWI structure along the (100) direction. A diagonal coordinate is introduced, in which the x axis is in the wire direction, and y and z axes are in the cross-sectional directions. An electric field F is

[a]Current address: Kansai Electronics Research Laboratory, NEC Corporation, 2-9-1, Seiran, Ohtsu 520, Japan.

 0021-8979/93/74(6)/3983/10/$6.00

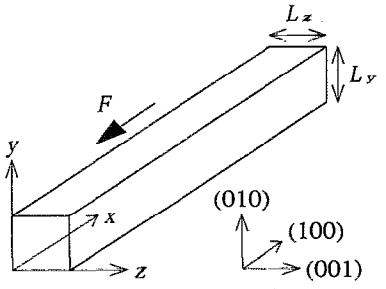

FIG. 1. Schematic representation of a QWI structure.

applied parallel to the x direction. L_x is the wire length, and L_y and L_z are the wire thicknesses in the y and z directions, respectively. In this simulation, $L_y = L_z = 3L_0$ is chosen with $L_0 = \sqrt{\hbar/2m^*_\Gamma\omega_{LO}}$ (≈ 40 Å for GaAs).[7] Here, m^*_Γ is the Γ-valley effective mass and ω_{LO} is the phonon frequency for the longitudinal optical (LO) modes.[7]

A. The 1-D subbands

Electrons are free to move in the x direction and are confined in the y and z directions by the infinite potential barrier. According to the effective mass approximation, the electron wave function $|m,n,k\rangle$ is given by

$$|m,n,k\rangle = \frac{\exp(ikx)}{\sqrt{L_x}}\sqrt{\frac{2}{L_y}}\sin\frac{m\pi y}{L_y}\sqrt{\frac{2}{L_z}}\sin\frac{n\pi z}{L_z}, \tag{1}$$

where k is the wave vector in the x direction, and m and n are the quantum indices for decoupled y- and z-electron states, respectively. Taking nonparabolicity into account, the associated energy $E_{mn}(k) = E_m + E_n + E(k)$ is obtained from

$$\gamma[E(k)] = \frac{\hbar^2k^2}{2m^*_x}, \tag{2a}$$

$$\gamma(E_m) = \frac{\pi^2\hbar^2m^2}{2m^*_yL_y^2}, \tag{2b}$$

and

$$\gamma(E_n) = \frac{\pi^2\hbar^2n^2}{2m^*_zL_z^2}. \tag{2c}$$

Here, $\gamma(E) = E(1+\alpha E)$, and α is assumed as 0.612 eV^{-1} for the Γ valley and is neglected for the L and X valleys. In these expressions, $m^*_\xi(\xi = x,y,z)$ is the conductivity electron mass along the ξ direction.

B. Anisotropic mass effects

We introduce the anisotropic effects in the L and X valleys. In the classical Monte Carlo simulations, the L and X minima are approximated by the spherical energy surfaces. This assumption is valid for the bulk systems in which electron motions are randomized in satellite valleys. For the extremely confined QWIs, where 1-D subbands are formed in the satellite valleys, the anisotropic effects take on an important role, since electron motions are collimated to one direction.

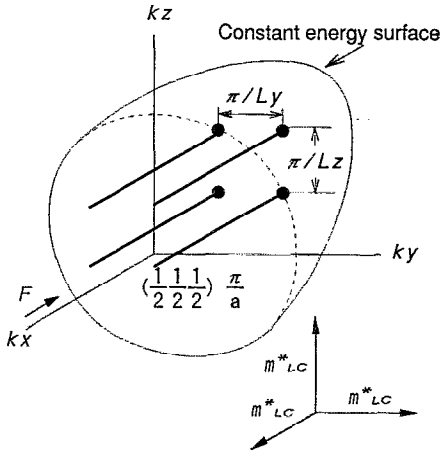

FIG. 2. Quantized electron states in the L valley for extremely confined QWI. The conductivity masses along x, y, and z directions are identical.

Figure 2 shows the quantized electron states in the L valley. The drift phenomena for L valley electrons traveling along the x direction are described in terms of the conductivity effective mass m^*_{LC}:[20]

$$m^*_{LC} = 3\left(\frac{2}{m^*_{Lt}} + \frac{1}{m^*_{Ll}}\right)^{-1}. \tag{3}$$

With $m^*_{Lt} = 0.075m_0$ and $m^*_{Ll} = 1.9m_0$ for GaAs,[21] m^*_{LC} is estimated to be $0.11m_0$, which is half of the density-of-state (DOS) effective mass for the L valley. This effect will improve electron transport characteristics at high fields. Regarding X valleys, as shown in Fig. 3, the equivalence of (100), (010), and (001) minima fails in extremely confined 1-D systems. In the (100) minimum, the conductivity masses along the x direction (m^*_x) and along the y and z directions (m^*_y and m^*_z) are m^*_{Xl} and m^*_{Xt}, respectively, while the former is $m^*_x = m^*_{Xt}$ in the (010) and the (001) minima. For GaAs, $m^*_{Xt} = 0.19m_0$ and $m^*_{Xl} = 1.9m_0$.[21] Con-

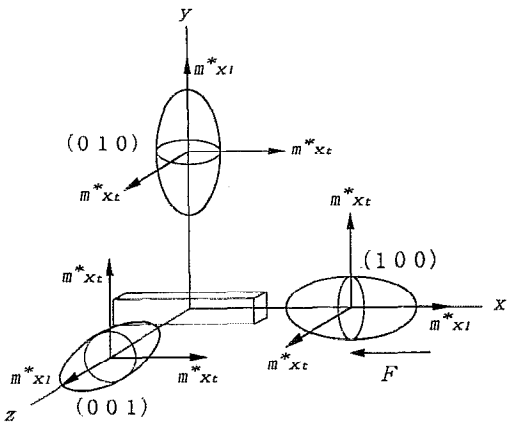

FIG. 3. Constant energy surfaces for the X valleys. The equivalence of the (100), (010), and (001) minima fails for extremely confined QWI.

sequently, the subband energies rise in the (100) minimum as compared to the (010) and (001) minima, although the conductivity mass along the wire orientation is larger in the (100) minimum than in the other minima.

III. SCATTERING RATES

According to the semiclassical approach, the transition probability $S_{\nu\nu'}(k,k',\mathbf{q})$ from the initial state $|\nu,k\rangle = |m,n,k\rangle$ to the final state $|\nu',k'\rangle = |m',n',k'\rangle$ mediated by a phonon $\mathbf{q}$ is given by

$$S_{\nu\nu'}(k,k',\mathbf{q}) = \frac{2\pi}{\hbar} |M_{\nu\nu'}(k,k',\mathbf{q})|^2 \times \delta[E_\nu(k') - E_\nu(k) \pm \hbar\omega_{\mathbf{q}}]. \quad (4)$$

Here, $M_{\nu\nu'}(k,k',\mathbf{q})$ is the electron-phonon matrix element. The $\pm$ sign denotes the emission (+) and absorption (−) of phonons. The corresponding scattering rate is

$$\lambda_{\nu\nu'}(k,k') = \frac{L_y L_z}{(2\pi)^2} \int dq_y\, dq_z\, S_{\nu\nu'}(k,k',\mathbf{q}). \quad (5)$$

To avoid the divergence in the scattering rate due to the 1-D DOS, we introduce the average scattering rate $\Lambda_{\nu\nu'}(k,k')$ defined by

$$\Lambda_{\nu\nu'}(k,k') = \frac{\int_{k-\Delta k/2}^{k+\Delta k/2} \lambda_{\nu\nu'}(k,k')\,dk}{\Delta k}. \quad (6)$$

The total scattering rate $1/\tau_\nu(k)$ from the initial state $|\nu,k\rangle$ is therefore

$$\frac{1}{\tau_\nu(k)} = \sum_{\nu' k'} \Lambda_{\nu\nu'}(k,k'). \quad (7)$$

The POP and intervalley phonon scatterings are included in this simulation. The POP scattering rates $\lambda^{(\mathrm{LO})}_{\nu\nu'}(k,k')$ are calculated as an extension of the pioneering work by Leburton.[7] In the first approximation, the overlap integrals are calculated using the classical formulation proposed by Fawcett *et al.*[22] As for the POP mechanism, only bulk LO modes are considered. The surface optical (SO) modes are not considered if the wire is thicker than 100 Å. The intervalley scattering rates of 2-D systems have been given by Ridley.[23] By modifying Ridley's method, the intervalley scattering rates $\lambda^{(ij)}_{\nu\nu'}(k,k')$ are calculated for 1-D systems. We use the intervalley deformation potentials obtained by Fischetti.[24] Expressions for $\lambda^{(\mathrm{LO})}_{\nu\nu'}(k,k')$ and $\lambda^{(ij)}_{\nu\nu'}(k,k')$ are summarized in Appendices A and B, respectively. This simulation is performed without the Coulomb scattering, since most experiments are done with modulation-doped materials. The electron-electron (*e-e*) scattering is also neglected. However, as Leburton and Jovanovic[17] pointed out, *e-e* scattering vanishes for 1-D intrasubband transitions, while for 1-D intersubband transitions, the *e-e* scattering rate becomes negligibly small. Figure 4 presents the scattering rate (300 K) for the Γ first subband. The origin of electron energies is set at the bottom of the conduction band. Peaks correspond to emission or absorption to the bottom of the subband. The main scattering mechanism below 0.3 eV is POP scatterings. Above 0.3 eV, the peaks are mainly due to the intervalley scatterings to the L and X valleys.

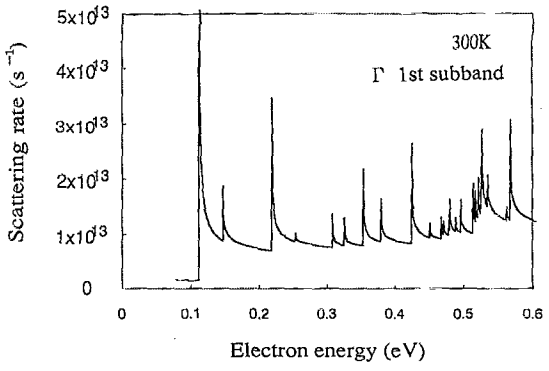

FIG. 4. Energy dependence of the 1-D scattering rate for the Γ first subband at 300 K.

IV. MONTE CARLO CODE

The EMC code was developed to simulate electron transports in QWIs. We simulated 32 subbands (the lowest 4 subbands in each valley). This allowed a realistic simulation because the average energy is less than 0.5 eV from the bottom of the conduction band. The scattering rates $\Lambda^{(\mathrm{LO})}_{\nu\nu'}(k,k')$ and $\Lambda^{(ij)}_{\nu\nu'}(k,k')$ between these subbands are tabulated as input to the EMC simulation. This requires limiting the simulated electron energy range. In this simulation, we considered energies less than 1 eV above the bottom of the conduction band. The direct integration method[16] was adopted for determining free-flight time. The major difference from the Briggs–Leburton method[16] consisted in the introduction of a constant momentum mesh. The momentum resolution is selected as $\delta k = qF\delta t/\hbar$, where δt is 1 fs or less. In each time step δt, the distribution function is calculated and the Pauli exclusion principle is considered by use of the rejection technique.[25] The cell size Δk for collecting distributions is 1.52×10^4/cm. The momentum distribution function $f_\nu(k)$ is calculated by making the ensemble average:

$$f_\nu(k) = \frac{\pi N_\nu(k) n_L}{N\Delta k}. \quad (8)$$

Here, $N_\nu(k)$ is the particle distribution, n_L is the line electron density, and N is the total particle number. For determining the steady-state distribution and the physical quantities, we considered both the ensemble and the time average. The synchronous ensemble method[16,26] is inappropriate as an extension to the transient or diffusion simulations since the sampling time is different between particles.

V. STEADY-STATE SIMULATION

For steady-state calculations, 1000 particles were simulated. The Fermi–Dirac (degenerate case) or Maxwellian (nondegenerate case) distribution was used for the initial condition. We simulated 5×10^5 scattering events for

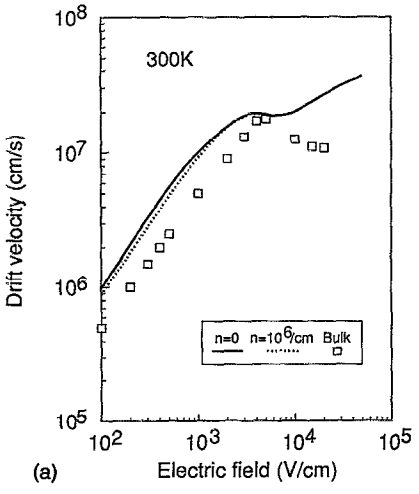

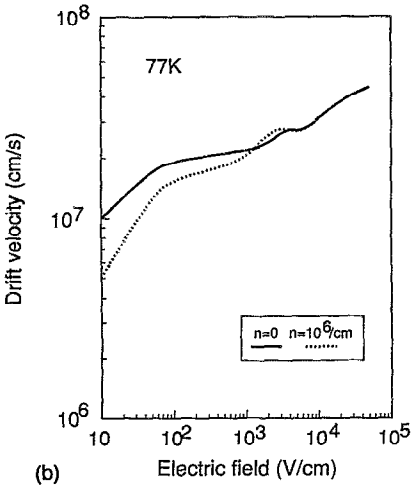

FIG. 5. Drift velocity vs electric field for nondegenerate (solid line) and degenerate (dotted line) QWIs at (a) 300 K and (b) 77 K. The squares denote bulk GaAs values [after Carnez (Ref. 29)].

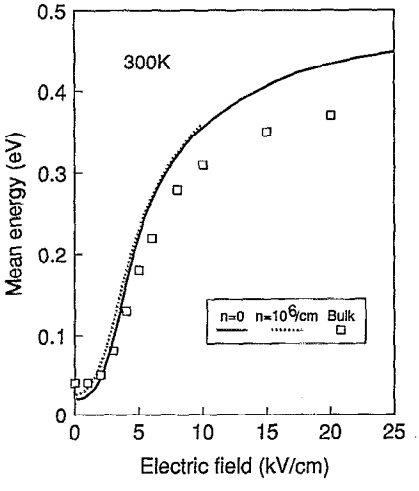

FIG. 6. Mean energy vs electric field for nondegenerate (solid line) and degenerate (dotted line) QWIs at 300 K. The squares denote bulk GaAs values [after Carnez (Ref. 29)].

achieving steady states. For the degenerate case, the line electron density was set at 1×10^6/cm, which is equivalent to the volume density of 7×10^{17}/cm^3.

A. Velocity- and energy-field relations

Figures 5(a) and 5(b) present velocity-field (v-F) characteristics at 300 and 77 K, respectively. The enhancement in the 1-D mobility is indicated for both temperatures. At 77 K, the nondegenerate mobility ($\approx10^6$ cm^2/V s) is twice as high as the POP-limited mobility for high-purity bulk GaAs ($\approx6\times10^5$ cm^2/V s).[27] The mobility enhancement at low temperature is related to a strong asymmetry in the momentum distribution functions mentioned later. The degeneracy effect reduces the low-field mobility significantly at low temperature. For high-field conditions, the v-F curves show a plateau at the critical field of the Γ-L transition (≈3 kV/cm) and a gradual increase as $F>10$ kV/cm. At $F=20$ kV/cm, 50% of the electrons are in L valleys while 35% are in X valleys. In this simulation, the conductivity mass $0.11m_0$ is adapted for L valleys. For studying the influence of the L valley mass value, we have also used the DOS effective mass value $0.22m_0$ instead of $0.11m_0$ for the EMC simulation as well as for scattering rate calculations. Here, v (300 K) is 1.9×10^7 cm/s at $F=20$ kV/cm. On the other hand, 2.7×10^7 cm/s is obtained by using $0.11m_0$ for the L valley mass [Fig. 5(a)]. Therefore, the high saturation velocity ($\approx3\times10^7$ cm/s) is due to the anisotropic mass effects in satellite valleys described in Sec. II B. This behavior should be distinguished from the velocity runaway effect that is indicated in the one-valley calculation by Yamada and Sone.[19] The velocity runaway effect, which is triggered by degeneracy, is hardly seen in our results, since hot electrons rapidly escape from a Γ valley with intervalley scatterings.

Figure 6 presents energy-field (E-F) characteristics at 300 K. The origin of the energies is set at the bottom of the first subband in the Γ valley. The degeneracy effect increases the average energy by less than 30 meV. In the nondegenerate QWI, the kinetic energy is 16 meV at $F=100$ V/cm. This value is equivalent to the electron temperature T_e of 360 K. The electron heating effect is emphasized at low temperature. At 77 K, the kinetic energy at $F=10$ V/cm is 8 meV, which corresponds to T_e of 190 K. These electron heating effects are related to the non-Maxwellian distribution functions that will be mentioned later.

B. Distribution functions

Figures 7 and 8 show the energy distribution functions $f_v(E)$ at equilibrium and at a low electric field ($F=100$ V/cm), respectively, for the Γ first subband. The origin of energies is set at the bottom of the conduction band. Equilibrium simulations for the nondegenerate and degenerate QWIs show the Maxwellian (Fig. 7) and the Fermi–Dirac distributions, respectively. However, once a low electric field is applied, the equilibrium condition rapidly breaks down so that structures in $f_v(E)$ appear at multiples of $\hbar\omega_{LO}$ [Fig. 8(a)]. The strong nonlinearity at thresholds of

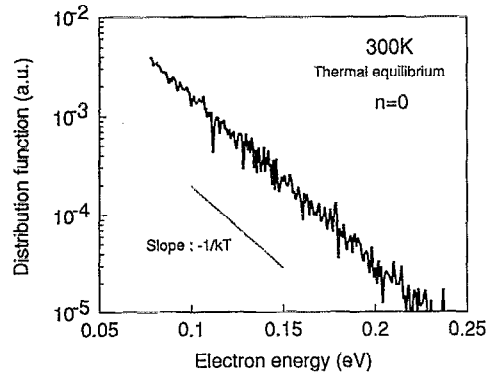

FIG. 7. Equilibrium energy distribution for the Γ first subband electrons at 300 K for a nondegenerate QWI.

the POP emissions is related to the divergence in emission rates due to the 1-D DOS, as pointed out by Briggs and Leburton.[16] The electron heating is caused by this non-Maxwellian distribution. At low temperature ($kT \ll \hbar\omega_{LO}$), the POP absorption rate is negligibly small compared to the POP emission rate. Due to the absence of POP absorptions and the divergence of emission rates, electrons drift periodically between the subband bottom and the POP emission threshold, as shown in Fig. 9. Due to this oscillation, the 77 K distribution function shows large gaps at the POP emission thresholds, as well as a strong asymmetry in the momentum direction [Fig. 8(b)]. This asymmetrical momentum distribution overly improves the 1-D mobility.

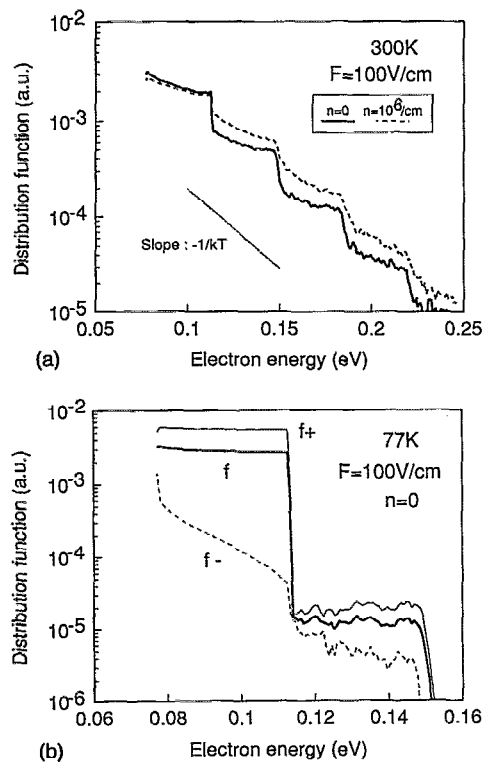

FIG. 8. Energy distribution function under an electric field of 100 V/cm for the Γ first subband electrons for QWI structures. (a) At 300 K for the nondegenerate (solid line) and degenerate (dotted line) QWIs. (b) At 77 K for a nondegenerate QWI; the average distribution (f), the distributions for the positive momentum (f_+) and for the negative momentum (f_-) are shown.

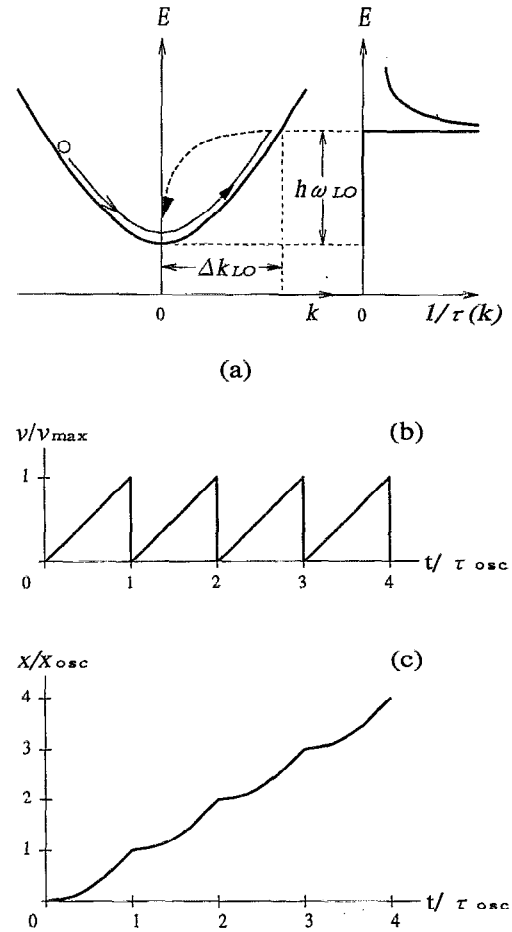

FIG. 9. The velocity oscillation mechanism at low temperature. (a) Schematic representation for the conduction band and the scattering rate of a QWI structure. Due to the absence of POP absorptions and a divergence of emission rates, electrons drift periodically between the subband bottom and the POP emission threshold. (b) The velocity of a particle as a function of time. The electron velocity shows oscillatory behavior with a time period τ_{osc}. (c) The path of the particle in real space. The electron shows a periodic trajectory with a time period τ_{osc}. Since each electron draws a similar trajectory, a periodic sequence of POP emissions introduces no carrier diffusion.

VI. TRANSIENT SIMULATION

The transient behaviors associated with the pulse and the step fields are simulated and were compared to results from the relaxation time approximation (RTA).

A. Relaxation times

According to the relaxation time approximation, hot electron transports can be described by the phenomenological momentum and energy balance equations:[28]

$$m^*_{SS}(E)\frac{dv}{dt}=qF-\frac{m^*_{SS}(E)v}{\tau_m(E)} \tag{9a}$$

and

$$\frac{dE}{dt}=qFv-\frac{E-E_0}{\tau_E(E)}. \tag{9b}$$

Here, E_0 is the reference energy, m^*_{SS} is the steady-state effective mass, and τ_m and τ_E are the momentum and energy relaxation times, respectively. The relaxation times are evaluated by[28]

$$\tau_m(E)=\frac{m^*_{SS}(E)v_{SS}(E)}{qF_{SS}(E)} \tag{10a}$$

and

$$\tau_E(E)=\frac{E-E_0}{qF_{SS}v_{SS}(E)}. \tag{10b}$$

Here, v_{SS} and F_{SS} are steady-state values for v and F, respectively, and can be taken from EMC results. For the degenerate QWI at 300 K, τ_m is close to 0.3–0.4 ps while τ_E typically ranges between 1 and 2 ps. With reducing temperature, τ_m increases ($\tau_m \approx 0.4$–0.6 ps at 77 K), while τ_E slightly decreases. Energy (E-E_0) dependence of m^*_{SS}, τ_m, and τ_E at 300 K is shown in Figs. 10(a), 10(b), and 10(c), respectively. For carrier energies $E>0.3$ eV, the τ_m has a peak in the 1-D system, while the bulk one decreases monotonically[29] [Fig. 10(b)]. Since τ_m is proportional to the steady-state momentum [Eq. (10a)], this increase in the 1-D relaxation time might be attributed to the momentum enhancement along the wire direction. For τ_E there is no significant difference between the 1-D and the bulk values, except near equilibrium [Fig. 10(c)]. In spite of the sharp energy dependence of the 1-D scattering rates, the relaxation times show rather light energy dependence. This discrepancy can be explained by the carrier heating effect. By increasing the electric field, the energy distribution function broadens so that effects of each singularity are weakened with the averaging between particles. At low field and/or low temperature, however, these smooth RTA functions cannot account for some of the sophisticated phenomena originating from the 1-D subbands (e.g., the velocity oscillation that will be discussed in Sec. VI C).

B. Velocity overshoot phenomena

The response to an electric field pulse is simulated with RTA. Equations (9a) and (9b) are solved by the Runge–Kutta method, combined with $m^*_{SS}(E)$, $\tau_m(E)$, and $\tau_E(E)$ functions deduced by steady-state simulations of the degenerate systems. The EMC technique is also applied to the same simulation. In accordance to the level of the applied field, the time resolution is selected (1 and 0.05 fs for 2 and 40 kV/cm, respectively). Starting with the steady-state distribution, the evolutions of electron states are simulated using 1000 particles. The velocity and energy are calculated by making the ensemble average at each 0.2 ps. Figures 11(a) and 11(b) show the time response of drift velocity and of energy, respectively, at 300 K. As discussed earlier, due to the considerably high electric field presumed in this simulation, the singularities in the 1-D scattering rates are expected to have little influence. A faster energy relaxation in the RTA result than in the EMC result [Fig. 11(b)] is caused by the lack of intervalley scatterings in the one-valley RTA model. By contrast, fairly good agreement of velocity relaxation [Fig. 11(a)] suggests that multivalley effects have less influence on momentum relaxation. The 1-D intervalley transitions occur most frequently at the

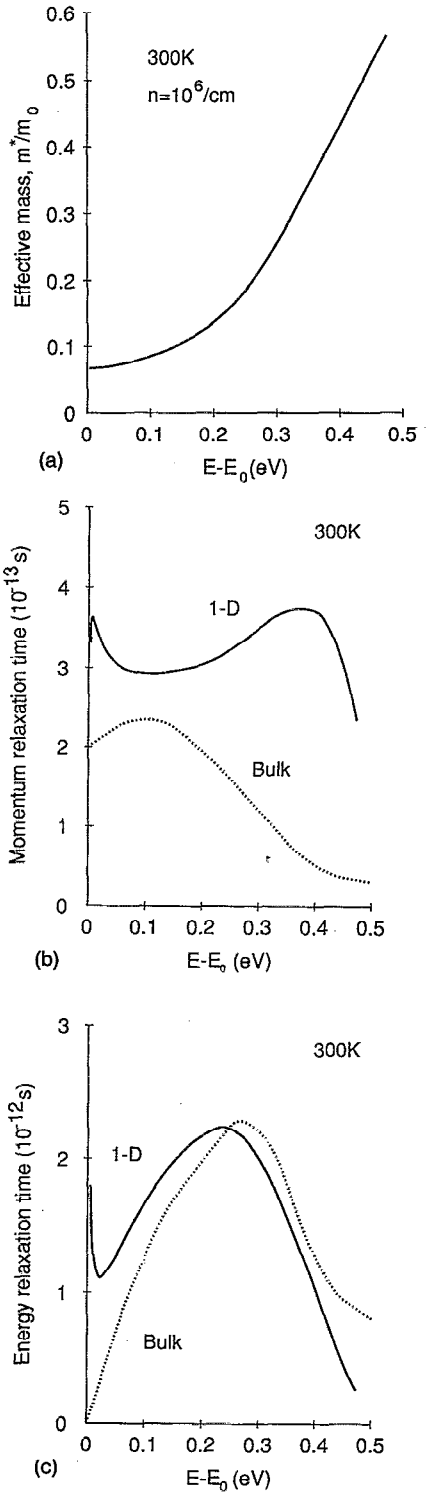

FIG. 10. Energy dependence of (a) effective mass, (b) momentum relaxation time, and (c) energy relaxation time for a degenerate QWI (solid lines) compared to bulk GaAs values (dotted lines) [after Carnez (Ref. 29)], at 300 K.

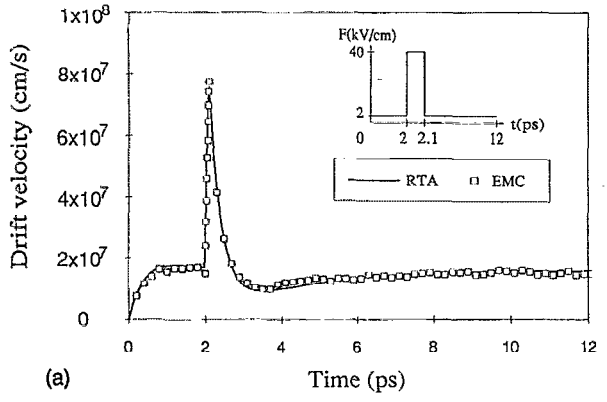

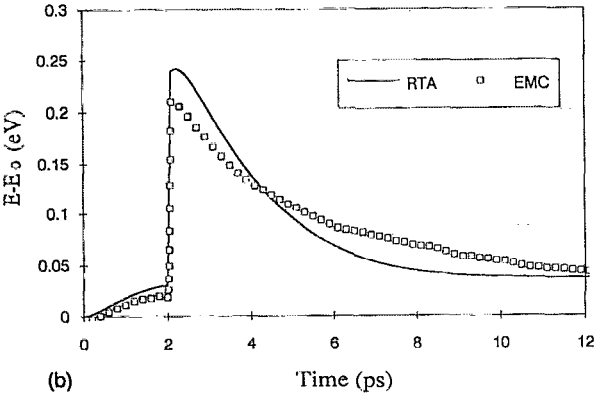

FIG. 11. Temporal variation of (a) drift velocity and (b) mean energy for an electric field pulse at 300 K, simulated for a degenerate QWI with RTA (solid lines) and EMC (squares) techniques.

bottoms of satellite valleys due to the $1/\sqrt{E}$ divergence in the DOS, but because of the identical rate for forward ($k=0$ to k') and backward ($k=0$ to $-k'$) scatterings, the momentum changes are canceled, and these transitions, therefore, hardly affect velocity relaxation. We obtained close agreement between the EMC and the RTA approaches in the 77 K results as well. The satisfactory agreement obtained between the EMC and the RTA results indicates a validity of the phenomenological approach to QWI structures. The phenomenological approach based on the RTA is suited to simulating electron transports in ultrasmall devices.[29–32]

C. Velocity oscillation at low temperature

At low temperature ($kT \ll \hbar\omega_{LO}$), the velocity for an electron oscillates as a function of time [Fig. 9(b)]. Since the thermal dispersion is small, the oscillations are observed for average velocity as well as for mean energy. If electrons were to travel quasiballistically below the POP emission threshold, the period of oscillation τ_{osc} could be estimated classically:

$$\tau_{osc}=\frac{\hbar\Delta k_{LO}}{qF}. \tag{11}$$

Here Δk_{LO} is the electron wave number at the POP emission threshold. For GaAs, $\tau_{osc}=1.7$ ps at $F=1$ kV/cm. The oscillatory behavior for velocity and energy are simulated with transient EMC. Starting from the thermal equilibrium, 1000 particles are accelerated with a step variation of electric fields. In Fig. 12, the time response of drift velocity is plotted for several electric field strengths at 77 K (for the nondegenerate case). The τ_{osc} values as well as an inversely proportional relationship between τ_{osc} and F can be explained by Eq. (11). The oscillatory behavior disappears when $F \gg 1$ kV/cm or $F \ll 100$ V/cm. In the former condition, electrons are pumped beyond the POP emission threshold, while in the latter condition, POP absorptions or other scatterings dominate the transport properties. Spatial oscillatory behavior based on similar mechanisms was recently reported by Leburton and Jovanovic.[17]

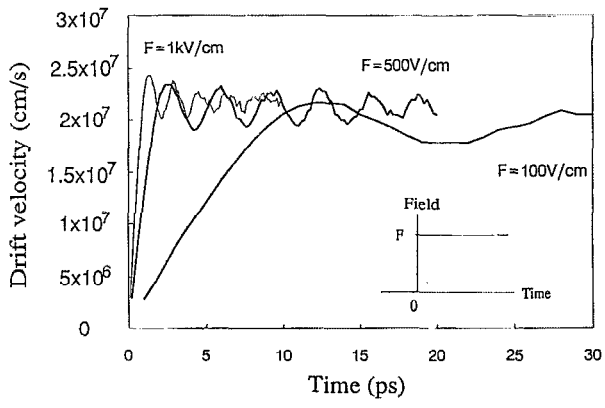

FIG. 12. Temporal variation of the drift velocity for electric field steps of 100, 500, and 1000 V/cm at 77 K, simulated for a nondegenerate QWI with an EMC technique.

VII. ELECTRON DIFFUSION

Electron diffusion phenomena are simulated using transient EMC with 1000 particles. After particles are placed at $x=0$ at the steady-state distribution, their displacements are simulated. In the low-frequency limit, the longitudinal diffusivity D_x is obtained from the variance of displacements, as is seen by[33]

$$D_x=\frac{\langle x^2\rangle-\langle x\rangle^2}{2\tau}, \tag{12}$$

where τ is the simulation time and the bracket represents an average over particles. There is no transverse diffusion in the extremely confined QWIs. We simulated 5×10^4–5×10^5 scattering events for an accurate estimation of D_x.

The diffusivity versus field relations at 300 and 77 K are shown in Figs. 13(a) and 13(b), respectively. For the nondegenerate QWI, calculated low-field diffusivities are approximately twice as high as the values obtained by the Einstein relation. The deviation from the Einstein relation results from the non-Maxwellian distribution along with the electron heating. In addition, the degeneracy effect generates additional carrier diffusion.[34] In comparison to bulk GaAs,[33] there is an important increase in the 1-D diffusivity at low fields. At high fields, the 1-D diffusivity is ap-

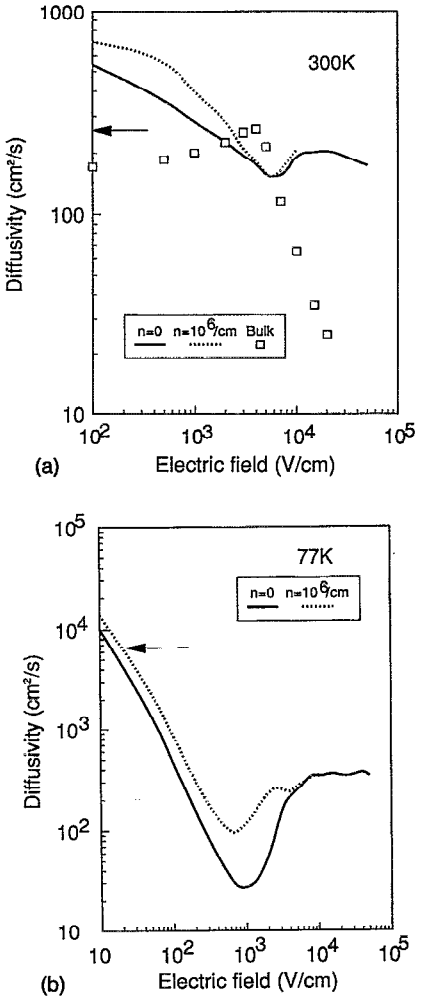

FIG. 13. Diffusivity vs electric field for the nondegenerate (solid line) and degenerate (dotted line) QWIs at (a) 300 K and (b) 77 K. The arrows indicate the low-field diffusivities obtained from the Einstein relation. The symbols (squares) denote bulk GaAs values [after Fauquembergue (Ref. 33)].

proximately 10 times as high as that of bulk values. These strong diffusions are consistent with low-field mobility and the saturation velocity enhancements of the 1-D system. The 77 K diffusivity shows a strong reduction near 1 kV/cm. We consider that the diminishing of D_x is related to the velocity oscillation effect. As indicated in Fig. 9(c), if the observation time is much longer than $\tau_{\rm osc}$, the drift velocity is assumed to be constant. Since each electron draws a similar trajectory in the x-t plane, no additional diffusion is introduced by a periodic sequence of POP emissions. We believe that the velocity oscillation effect at low temperature suppresses the diffusion noise by assisting quasiballistic transports.

VIII. CONCLUSIONS

EMC simulations have been performed for a GaAs (100) oriented square well wire with a cross section of 120×120 Å^2. The model considers the infinite potential approximation as well as the extreme confinement limit. At low fields, the non-Maxwellian distribution, originating from the 1-D DOS, leads to some distinctive features (mobility enhancement, electron heating, and deviation from the Einstein relation). On the other hand, the anisotropic effects of L valleys play an important role for high-field behavior (velocity enhancement and diffusivity increase). Transient simulations at 77 K show the velocity oscillation. This result suggests the possibility of nondiffusive transport at low temperature. Hence, QWI structures seem to have very attractive features for microwave and millimeterwave applications. Finally, the satisfactory agreement obtained by transient EMC and the RTA results gives credence to the phenomenological approach to QWI devices. Results related to dc, small-signal, and noise performance of QWI devices will be presented elsewhere.

ACKNOWLEDGMENTS

The authors would like to thank Professor G. Salmer for his encouragement. They would like to thank Professor R. Fauquembergue, Professor J. Zimmermann, Dr. G. Dambrine, Dr. H. Happy, Dr. F. Danneville, Dr. P. Win, S. Bollaert, Dr. J. L. Thobel, and Dr. L. Baudry for their fruitful discussions and help. One of the authors thanks Dr. H. Abe, Dr. M. Kuzuhara, and Dr. N. Samoto of NEC for their encouragement.

APPENDIX A: 1-D POP SCATTERING RATES

Extending Leburton's method,[7] one can calculate the intersubband POP scattering rates for 1-D systems. The scattering rates $\lambda^{(\rm LO)}_{\nu\nu'}(k,k')$ for POP emission and absorption are expressed by

$$\lambda^{(\rm LO)}_{\nu\nu'}(k,k')=\frac{q^2\sqrt{m^*}\omega_{\rm LO}}{8\sqrt{2}\pi^2\hbar}\left(\frac{1}{\epsilon_\infty}-\frac{1}{\epsilon_0}\right)\left(n_{\rm LO}+\frac{1}{2}\pm\frac{1}{2}\right)\times\frac{1+2\alpha E(k')}{\sqrt{\gamma[E(k')]}}\{I^{\rm 1D}_{\nu\nu'}(q_x^+)+I^{\rm 1D}_{\nu\nu'}(q_x^-)\}G[E(k),E(k')], \quad \text{(A1)}$$

where the $\pm$ sign denotes the emission $(+)$ and absorption $(-)$ of phonons. $E(k)$ is the kinetic energy defined by (2a), ϵ_∞ and ϵ_0 are the optical and static dielectric constants, respectively, and $n_{\rm LO}$ is the excited phonon number obtained from Bose–Einstein statistics. In the first approximation, the overlap integral $G[E(k),E(k')]$ is calculated

using the classical expressions proposed by Fawcett *et al.*[22] From the momentum conservation, the allowed phonon wave vectors $q_x^{\pm}$ are

$$q_x^{\pm}=\begin{cases} k\left(1\pm\sqrt{\dfrac{\gamma[E(k')]}{\gamma[E(k)]}}\right):\text{emission} \\ k\left(-1\pm\sqrt{\dfrac{\gamma[E(k')]}{\gamma[E(k)]}}\right):\text{absorption.}\end{cases} \tag{A2}$$

Integral $I_{\nu\nu'}^{1D}$ is defined by

$$I_{\nu\nu'}^{1D}(q_x)=\int_{-\infty}^{\infty} dq_y\,dq_z\,\frac{|F_{mm'}(q_y)|^2|F_{nn'}(q_z)|^2}{|\mathbf{q}|^2}, \tag{A3}$$

with

$$F_{mm'}(q_y)=\frac{2}{L_y}\int_0^{L_y} dy \times\exp(-iq_y y)\sin\left(\frac{m\pi y}{L_y}\right)\sin\left(\frac{m'\pi y}{L_y}\right). \tag{A4}$$

The function $F_{mm'}$ can be calculated analytically, so that

$$|F_{mm'}(q_y)|^2=\begin{cases}\dfrac{\sin^2(q_yL_y/2)}{(q_yL_y/2)^2}\left\{\dfrac{(m-m')^2\pi^2}{q_y^2L_y^2-(m-m')^2\pi^2}+\dfrac{(m+m')^2\pi^2}{(m+m')^2\pi^2-q_y^2L_y^2}\right\}^2 :m-m'=\text{even} \\ \dfrac{\cos^2(q_yL_y/2)}{(q_yL_y/2)^2}\left\{\dfrac{(m-m')^2\pi^2}{q_y^2L_y^2-(m-m')^2\pi^2}+\dfrac{(m+m')^2\pi^2}{(m+m')^2\pi^2-q_y^2L_y^2}\right\}^2 :m-m'=\text{odd}\end{cases}. \tag{A5}$$

Furthermore, (A3) is rewritten as

$$I_{\nu\nu'}^{1D}(q_x)=2\int_0^{\infty} dq_y|F_{mm'}(q_y)|^2I_{nn'}^{2D}(q_x,q_y), \tag{A6}$$

where $I_{nn'}^{2D}=\int_{-\infty}^{\infty}dq_z|F_{nn'}(q_z)|^2/|\mathbf{q}|^2$. Inserting (A5), an explicit expression is obtained for $I_{nn'}^{2D}$:

$$I_{nn'}^{2D}(q_x,q_y)=\frac{\pi L_z}{4}\left\{\frac{1+\delta_{nn'}+(C^-+B^-/A^-)G^{\mp}}{A^-}+\frac{1+(C^++B^+/A^+)G^{\mp}}{A^+}\right\}, \tag{A7}$$

where the $\mp$ sign in $G^{\mp}$ denotes the cases where $n-n'$ is even $(-)$ or odd $(+)$. In the expression,

$$A^{\mp}=\frac{(n\mp n')^2\pi^2}{4}+S^2, \tag{A8a}$$

$$B^{\mp}=\frac{(n\mp n')^2\pi^2}{4}-S^2, \tag{A8b}$$

$$C^{\mp}=3\mp\frac{(n\pm n')^2}{nn'}, \tag{A8c}$$

and

$$G^{\mp}=\frac{1\mp\exp(-2S)}{2S}, \tag{A9}$$

with

$$S=\frac{\sqrt{q_x^2+q_y^2}}{2}L_z. \tag{A10}$$

Consequently, $\lambda_{\nu\nu'}^{(LO)}(k,k')$ is calculated by (A1) with (A2), and (A6)–(A10).

APPENDIX B: 1-D INTERVALLEY SCATTERING RATES

The 1-D intervalley scattering rates are calculated by modifying Ridley's 2-D model.[23] Neglecting a plurality of equivalent final valleys, the intervalley scattering rate $\lambda_{\nu\nu'}^{(ij)}(k,k')$ is expressed by

$$\lambda_{\nu\nu'}^{(ij)}(k,k')=\frac{\Xi_{ij}^2\sqrt{m_j^*}}{8\sqrt{2}\pi^2\hbar\omega_{ij}\rho}\left(n_{ij}+\frac{1}{2}\pm\frac{1}{2}\right)\frac{1+2\alpha_jE_j(k')}{\sqrt{\gamma[E_j(k')]}}\cdot 2J_{\nu\nu'}^{1D}\cdot G_{ij}[E_i(k),E_j(k')]. \tag{B1}$$

Here, ρ is the crystal density, Ξ_{ij} is the deformation potential, ω_{ij} is the intervalley phonon frequency, n_{ij} is the excited phonon number, and $G_{ij}[E_i(k),E_j(k')]$ is the overlap integral. Subscripts i and j attached on m^*, α, and $E(k)$ refer to the initial and final valleys, respectively. $J_{\nu\nu'}^{1D}$ is defined by

$$J_{\nu\nu'}^{1D}=\int_{-\infty}^{\infty} dq_y\,dq_z|F_{mm'}(q_y)|^2|F_{nn'}(q_z)|^2, \tag{B2}$$

where $F_{mm'}(q_y)$ is defined by (A4). Inserting (A5) into (B2), one obtains an explicit expression for $J_{\nu\nu'}^{1D}$:

$$J_{\nu\nu'}^{1D}=\frac{(2\pi)^2}{L_yL_z}\left(1+\frac{1}{2}\delta_{mm'}\right)\left(1+\frac{1}{2}\delta_{nn'}\right). \tag{B3}$$

[1] D. B. Rensch, D. S. Matthews, M. W. Utlaut, M. D. Courtney, and W. M. Clark, IEEE Trans. Electron. Devices **ED-34**, 2232 (1987).

[2] K. Ismail, W. Chu, D. A. Antoniadis, and H. I. Smith, J. Vac. Sci. Technol. B **6**, 1824 (1988).

[3] K. Tsubaki, T. Fukui, Y. Tokura, H. Saito, and N. Susa, Electron. Lett. **24**, 1267 (1988).

[4] K. Onda, F. Nihey, N. Samoto, M. Kuzuhara, Y. Makino, E. Mizuki, and T. Itoh, *1989 International Electron Devices Meeting Technical Digest*, 3–6 Dec., 1989, Washington, DC (IEEE, New York, 1989), p. 125.

[5] S. Bollaert, P. Legry, P. Win, H. Happy, and A. Cappy, *Proceedings of*

the 22nd European Solid State Research Conference, Leuven, 14–17 Sept., 1992 (Elsevier, New York, 1992), p. 325.
[6]H. Sakaki, Jpn. J. Appl. Phys. **19**, L735 (1980).
[7]J. P. Leburton, J. Appl. Phys. **56**, 2850 (1984).
[8]D. Ahn, J. Appl. Phys. **69**, 3596 (1991).
[9]K. W. Kim, M. A. Stroscio, A. Bhatt, R. Mickevicius, and V. M. Mitin, J. Appl. Phys. **70**, 319 (1991).
[10]V. K. Arora, Phys. Rev. B **23**, 5611 (1981).
[11]J. Lee and H. N. Spector, J. Appl. Phys. **54**, 3921 (1983).
[12]G. Fishman, Phys. Rev. B **34**, 2394 (1986).
[13]P. Yuh and K. L. Wang, Appl. Phys. Lett. **49**, 1738 (1986).
[14]S. DasSarma and X. C. Xie, Phys. Rev. B **35**, 9875 (1987).
[15]A. Ghosal, D. Chattopadhyay, and A. Bhattacharyya, J. Appl. Phys. **59**, 2511 (1986).
[16]S. Briggs and J. P. Leburton, Phys. Rev. B **38**, 8163 (1988).
[17]J. P. Leburton and D. Jovanovic, Semicond. Sci. Technol. **7**, B202 (1992).
[18]R. Mickevicius, V. V. Mitin, K. W. Kim, and M. A. Stroscio, Semicond. Sci. Technol. **7**, B299 (1992).
[19]T. Yamada and J. Sone, Phys. Rev. B **40**, 6265 (1989).
[20]B. R. Nag, in *Electron Transport in Compound Semiconductors* (Springer, Berlin, 1980).
[21]J. S. Blakemore, J. Appl. Phys. **53**, R123 (1982).
[22]W. Fawcett, A. D. Boardman, and S. Swain, J. Phys. Chem. Solids **31**, 1963 (1970).
[23]B. K. Ridley, J. Phys. C **15**, 5899 (1982).
[24]M. V. Fischetti, IEEE Trans. Electron. Devices **38**, 634 (1991).
[25]P. Lugli and D. K. Ferry, IEEE Trans. Electron. Devices **ED-32**, 2431 (1985).
[26]P. J. Price, IBM J. Res. Dev. **14**, 12 (1970).
[27]G. E. Stillman and C. M. Wolfe, Thin Solid Films **37**, 69 (1976).
[28]M. Shur, Electron. Lett. **12**, 615 (1976).
[29]B. Carnez, A. Cappy, A. Kaszynski, E. Constant, and G. Salmer, J. Appl. Phys. **51**, 784 (1980).
[30]A. Cappy, A. Vanoverschelde, M. Schortgen, C. Versnaeyen, and G. Salmer, IEEE Trans. Electron. Devices **ED-32**, 2787 (1985).
[31]A. Cappy, IEEE Trans. Microwave Theory Tech. **36**, 1 (1988).
[32]H. Happy, O. Pribetich, G. Dambrine, J. Alamkan, Y. Cordier, and A. Cappy, *1991 Institute of Electrical and Electronic Engineers Microwave Theory and Technology Society International Microwave Symposium Digest*, Boston, 10–14 June, 1991 (IEEE, New York, 1991), p. 627.
[33]R. Fauquembergue, J. Zimmermann, A. Kaszynski, and E. Constant, J. Appl. Phys. **51**, 1065 (1980).
[34]B. Mitra and K. P. Ghatak, Solid-State Electron. **32**, 810 (1989).